Source of Bright Luminescence in Gold Nanoclusters

Qi Li[1#*], Charles J. Zeman IV[2#], George C. Schatz[2], and X. Wendy Gu[1*]

[1]Department of Mechanical Engineering, Stanford University, Stanford, CA 94305, United States
[2]Department of Chemistry, Northwestern University, Evanston, IL 60208, United States

Abstract

Gold nanoclusters with near-infrared (NIR) photoluminescence (PL) have great potential as sensing and imaging materials in biomedical and bioimaging applications. In this work, Au_{21}(S-Adm)$_{15}$ and $Au_{38}S_2$(S-Adm)$_{20}$ are used to unravel the underlying mechanisms for the improved quantum yields (QY), large Stokes shifts and long PL lifetimes in gold nanoclusters. Both nanoclusters show decent PL QY. In particular, the $Au_{38}S_2$(S-Adm)$_{20}$ nanocluster shows a bright NIR PL at 900 nm with QY up to 15% in normal solvents (such as toluene) at ambient conditions. The relatively lower QY for Au_{21}(S-Adm)$_{15}$ (4%) compared to $Au_{38}S_2$(S-Adm)$_{20}$ is attributed to the lowest-lying excited state being symmetry-disallowed, as evidenced by the pressure-dependent anti-spectral shift of the absorption spectra compared to PL. Yet, Au_{21}(S-Adm)$_{15}$ maintains some emissive properties due to a nearby symmetry-allowed excited state. Furthermore, our results show that suppression of non-radiative decay due to the surface "lock rings", which encircle the Au kernel and the surface "lock atoms" and bridge the fundamental Au-kernel units (*e.g.,* tetrahedra, icosahedra, *etc.*), is the key to obtain high QYs in gold nanoclusters. The complicated excited-state processes and the small absorption coefficient of the band-edge transition lead to the large Stokes shifts and the long PL lifetimes that are widely observed in gold nanoclusters.

Keywords

Gold Nanoclusters, NIR emissions, Structure-Property Relations, Improvement of PL Efficiency, High-Pressure

1. Introduction

Gold and other metal nanoclusters show intriguing near-infrared (NIR) photoluminescence (PL)[1–9] that is different from conventional quantum dots and organic dyes. Particularly, many gold nanoclusters show relatively long PL lifetime from tens of nanoseconds to several microseconds and large Stokes shifts which are usually more than 0.3 eV.[10–15] Such features make gold nanoclusters, which are generally biocompatible and non-toxic, promising candidates for bioimaging and biosensing applications.[16–19] However, the reported PL quantum yields (QY) of most gold nanoclusters are very low. In the past decade, several strategies for the improvement of the PL efficiency of gold nanoclusters have been reported. For example, Wang *et al.*[20] reported that the QY of rod-shaped Au_{25} nanocluster can be substantially improved by heterometal doping and this doping-induced enhancement has also been verified by the Tsukuda[21] and Bakr[22] groups. Significant enhancement of PL by rigidifying the surface of the nanocluster was first reported by the Lee group[15], and the surface-regulated PL enhancement was reported from the Millstone[23], Tsukuda[24] and Wu[25] groups. Aggregation–induced–emission was introduced by the Xie group[26] and such a phenomenon was also reported by the Zhu[27], Konishi[28] and Wu[29] groups. Recently, Narouz *et al*[30] reported a highly luminescent Au_{13} nanocluster protected by n-heterocyclic carbenes which shows a 16% QY in solvent. In addition, the Aikens group conducted a series of computational studies on the mechanism of the PL enhancement in gold nanoclusters.[2,31,32] In our previous studies, significant enhancement of the PL QY was achieved by tailoring the surface structures,[11,33] embedding nanoclusters into polymers,[12] and dissolving the nanocluster in viscous solvents.[10] Most notably, our recent results show that the PL of gold nanoclusters can be significantly enhanced by increasing pressure.[34]

Despite these research advances, there is still a pressing need to elucidate the fundamental origins of common PL characteristics (*e.g.,* large Stokes shifts and long PL lifetime) towards a precise control of gold nanoclusters' PL properties, and to determine some general structure-design strategy for a rational improvement of their PL efficiencies. Furthermore, although QYs up to 20% to 60% have been recently reported under specific conditions (*e.g.,* in viscous solvents,[10] micelles,[15] and solid matrix[12]), NIR-emitting gold nanoclusters, especially thiolate-protected gold nanoclusters ($Au_m(SR)_n$), commonly show low QY (< 1%) in normal solvents and ambient environments. This work starts from a spectroscopic study of a *quasi*-cuboctahedral nanocluster, Au_{21}(S-Adm)$_{15}$ (S-Adm = 1-admantanethiolate), which has a ~4% QY. Our results show that the

replacement of a single Au atom with a S atom in the mono-cuboctahedral kernel significantly alters the excited-state dynamics such that an excited-state transition between two energetically similar electronic states is observed. Our results further suggest that *i)* the complicated excited-state processes and *ii)* the low absorption coefficient of the band-edge transition induce the commonly observed PL characteristics of gold nanoclusters, including large Stokes shifts and long PL lifetime. We report that by tailored suppression of these properties, the *bcc* $Au_{38}S_2(S\text{-}Adm)_{20}$ nanocluster shows PL at 910 nm with QY up to 15% in normal solvents and ambient conditions.

2. Results and Discussions

2.1. Spectroscopic Study of $Au_{21}(S\text{-}Adm)_{15}$

Figure 1 displays the optical properties of $Au_{21}(S\text{-}Adm)_{15}$ in ambient conditions. The single-crystal X-ray structure of $Au_{21}(S\text{-}Adm)_{15}$ is first shown in Figure 1A. The $Au_{21}(S\text{-}Adm)_{15}$ nanocluster consists of a *quasi*-cuboctahedral "13-1+2" gold kernel in which one gold atom is replaced with sulfur in the bottom layer (Anatomy of the atomic structure is in Figure S1). Three gold tetrahedral units can also be found in $Au_{21}(S\text{-}Adm)_{15}$ nanocluster and one sulfur atom (black dashed circles in Figure 1A) bridges two tetrahedra which acts as a lock to fix the kernel. Another prominent structural feature of $Au_{21}(S\text{-}Adm)_{15}$ is that a Au_8S_9 "lock ring" can be found (black dashed circles in Figure 1A) on the surface. The absorption spectrum of $Au_{21}(S\text{-}Adm)_{15}$ is displayed in Figure 1B and a prominent absorption peak at 690 nm is observed. The PL spectrum of $Au_{21}(S\text{-}Adm)_{15}$ is shown in Figure 1C and one major peak at ~820 nm is observed. The stokes shift of $Au_{21}(S\text{-}Adm)_{15}$ is calculated to be ~0.3 eV. The PL excitation spectrum is shown in Figure S2, which shows a shape similar to the absorption. The PL quantum yields (QYs) of $Au_{21}(S\text{-}Adm)_{15}$ in various solvents such as DCM and toluene are ~4 %, which are higher than other cuboctahedral $Au_m(SR)_n$ nanoclusters.[12]

The excited-state dynamics of $Au_{21}(S\text{-}Adm)_{15}$ are studied by time-correlated-single-photon-counting (TCSPC) and femtosecond transient absorption (fs-TA) spectroscopy. The excited-state features of $Au_{21}(S\text{-}Adm)_{15}$ are also significantly different from *fcc* mono-cuboctahedral nanoclusters,[12] though their structures are quite similar. Figure 1D shows the TCSPC trajectory of $Au_{21}(S\text{-}Adm)_{15}$ which was detected at ~830 nm. Three lifetime components: 1.5 ns, 793.4 ns and 2.8 μs can be identified. fs-TA spectra are shown in Figure 1E. A broad and strong excited state absorption (ESA) centered at 620 nm is observed which decays from ~100 ps to 7 ns. Meanwhile, the ground-state bleach around 500 nm remains relatively constant. This result indicates a state-

transition in this time range which is consistent with the 1.5 ns component in TCSPC measurement. A schematic diagram of the electronic transitions and the two-emission model of $Au_{21}(S\text{-}Adm)_{15}$ is shown in Figure 1F. It should be noted that $Au_{21}(S\text{-}Adm)_{15}$ does not show significant dual-emission unlike bi-tetrahedral nanoclusters.[10] This can be ascribed to the two-states being so close in energy that only one major peak can be identified in the steady-state PL spectrum.

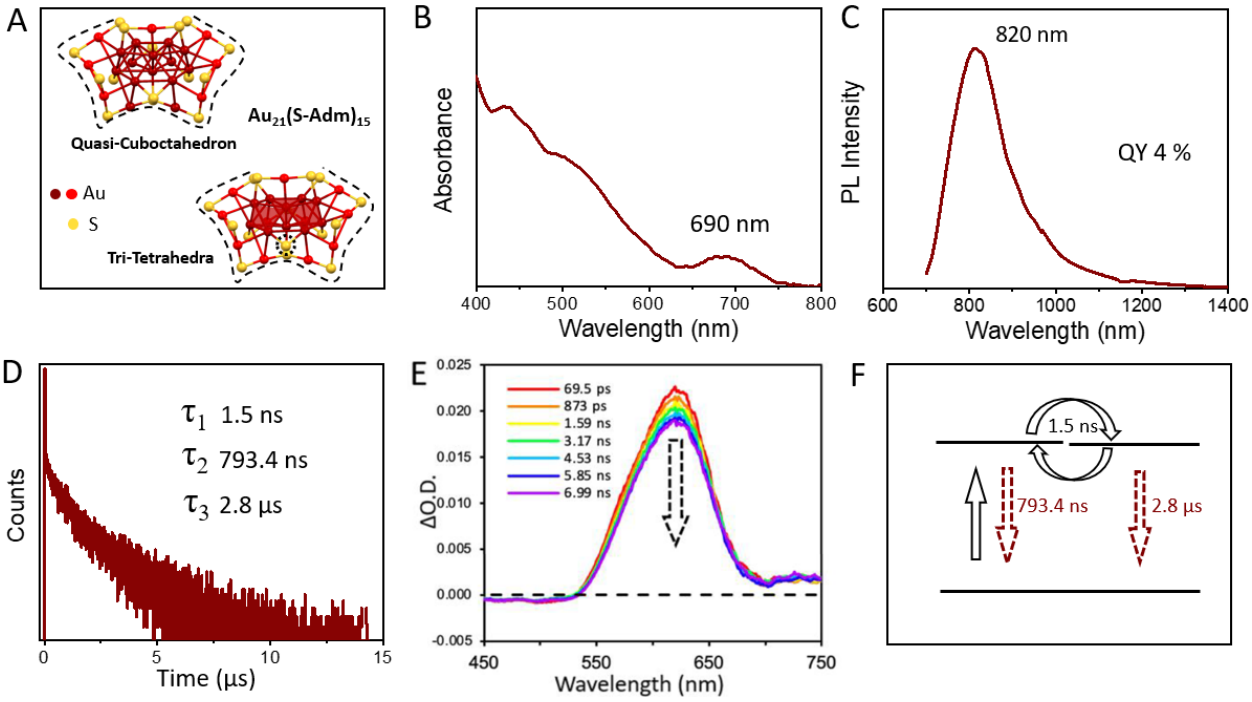

Figure 1. Optical Properties of $Au_{21}(S\text{-}Adm)_{15}$. (A) Atomic structure determined from single-crystal diffraction. (B) Absorption spectrum. (C) PL spectrum (excited at 500 nm). (D) TCSPC trajectory. (E) Transient absorption spectra. (F) Schematic diagram of the electronic transitions and the two-emission-state model.

To obtain more insight into the excited-state transition and PL mechanism, we measured the absorption and PL of $Au_{21}(S\text{-}Adm)_{15}$ in different solvents. As shown in Figure S3 and S4, $Au_{21}(S\text{-}Adm)_{15}$ shows minor changes in absorption and PL when dissolved in various solvents with different polarities and viscosities. This result indicates that the structural transformation and charge transfer process that is prominent in bitetrahedral nanoclusters,[10] is not significant in $Au_{21}(S\text{-}Adm)_{15}$. We further used the framework developed in our previous work[35] to analyze the relation of PL and absorption transition in $Au_{21}(S\text{-}Adm)_{15}$. The absorption coefficient (ε) of $Au_{21}(S\text{-}Adm)_{15}$ at 690 nm is calculated to be ~5.3×10^3 $cm^{-1}M^{-1}$ and the "intrinsic" radiative lifetime τ of the 690 nm transition in $Au_{21}(S\text{-}Adm)_{15}$ in the order of hundreds of ns which is two orders of magnitude longer than the 1.5 ns PL lifetime component, indicating that the 1.5 ns process should

be ascribed to a nonradiative process. This result further justifies the two-state model from the time-resolved experimental measurements (Figure 1F) in which the ~ 1.5 ns state-transition induces the second state with a longer 2.2 µs lifetime.

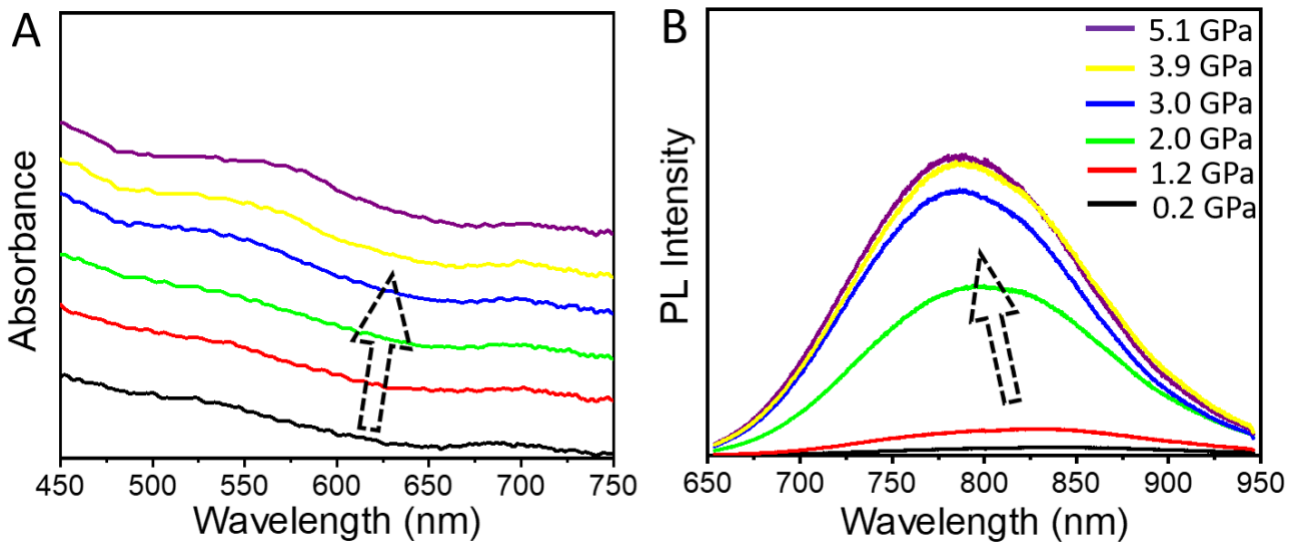

Figure 2. High-Pressure Optical Study of $Au_{21}(S\text{-}Adm)_{15}$. (A) Pressure-dependent absorption and (B) PL spectra in 2-ethylcyclohexane.

High-pressure optical studies were conducted to unravel the PL mechanism of $Au_{21}(S\text{-}Adm)_{15}$. **Figure 2** displays the pressure-dependent absorption and PL spectra of $Au_{21}(S\text{-}Adm)_{15}$ which are measured in a quasi-hydrostatic medium: 2-ethylcyclohexane. The absorption peak at ~690 nm continuously red-shifts as the pressure increases from 0.2 to 5.1 GPa. This pressure-induced red-shift in absorption is similar to the previous results for the *fcc*[12] and bitetrahedral[10] nanoclusters. The PL shows a blue-shift with an increase in pressure. PL intensity increases by a factor of ~40. Similar pressure-dependence was observed in toluene, a non-hydrostatic pressure medium (Figure S5). The opposing trends between the first absorption peak and the PL peak in $Au_{21}(S\text{-}Adm)_{15}$ indicate that their underlying electronic transitions are different.

Density functional theory (DFT) was used to explain the PL mechanisms and pressure-dependence of $Au_{21}(S\text{-}Adm)_{15}$ (**Figure 3**). The optimized BP86 ground state geometry gave an average Au-Au bond length for the *quasi*-cuboctahedral kernel of 2.9+/-0.2 Å, in good agreement with the known Au-Au bond length of bulk fcc gold of 2.872 Å, but slightly larger than what was found from the crystal structure (2.74+/-0.02 Å). Such deviations are expected with BP86, but cab still accurately predict spectral properties in other gold nanoclusters. The calculated electronic

spectra for $Au_{21}(S\text{-}Adm)_{15}$ are shown in Figure 3A where it can be seen that the low-energy absorption exhibits a collection of excitations in the range of 674 nm to 790 nm that are assigned to the lowest energy absorption band observed experimentally. Notably, these excitations for $Au_{21}(S\text{-}Adm)_{15}$ are resolved as two distinct peaks in the Gaussian-convoluted (black line, FWHM = 0.16 eV) absorption spectrum. Contrarily, in the calculations on structures derived from condensed-phase simulations (Fig. 3B, violet line), these excitations overlap sufficiently to give a single, broad absorption band at 0 GPa (*vide infra*). The greater overlap between S_1 and S_2 for condensed-phase structures is attributed to the bulkier S-Adm ligands, which were reduced to S-CH_3 for gas-phase calculations. The S-Adm ligands were associated with a mild (< 0.05 Å) decrease in Au-Au and Au-S bond lengths and shifts S_1 to higher energy. It is worth noting that previous theoretical work from the Zhu group found that C and H have negligible contributions to the frontier orbitals in $Au_{21}(S\text{-}Adm)_{15}$.[36] The calculated fluorescence energy was taken as the sum of the excitation energy and the total energy in the optimized excited state geometry of S_1, minus the total energy of the optimized ground-state geometry, which corresponds to the $E_{0\text{-}0}$ transition.[37,38] Such methods were shown in previous work to give accurate and predictive fluorescence energies.[35] This gave a wavelength of fluorescence of 928 nm, which corresponds to a Stokes shift of 0.23 eV. Although the agreement between the calculated and experimental Stokes shift (0.3 eV) is good, the low calculated absorption and fluorescence energy relative to experiment is an indicator that S_1 is not the sole-contributor to the observed PL.

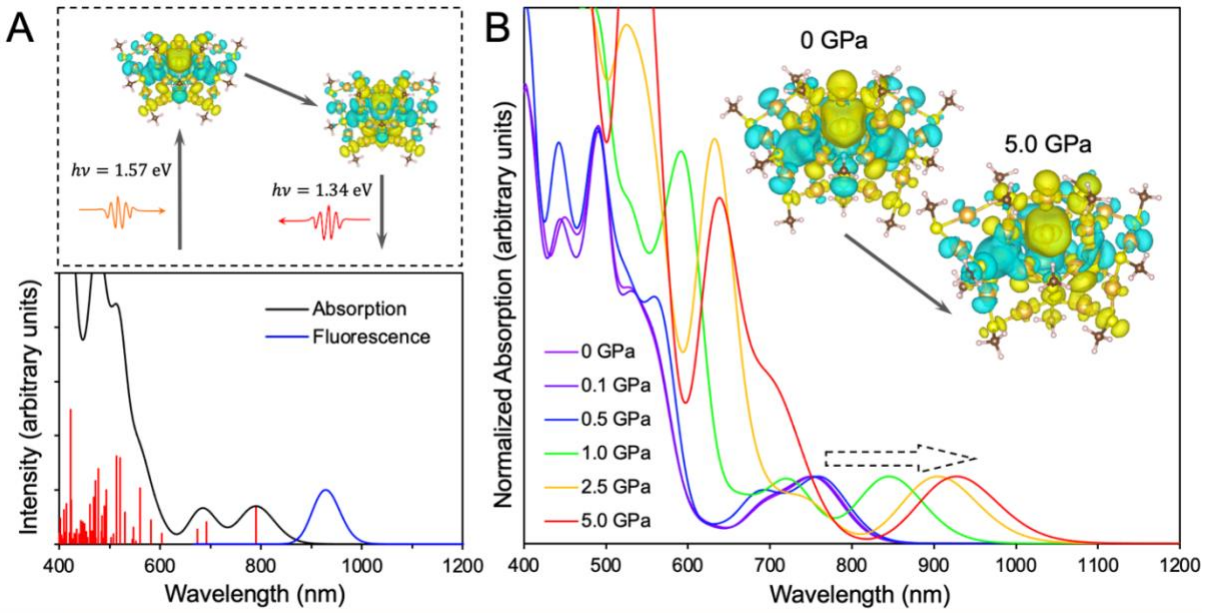

Figure 3. (A) Calculated absorption (black) and fluorescence (blue) spectra of $Au_{21}(S\text{-}Adm)_{15}$ where red lines show the stick spectrum of individual excitations. The top box shows the charge difference densities (CDDs) of S_1 in the ground state geometry and the relaxed excited-state geometry *via* a simplified Jablonski diagram. (B) Calculated absorption spectra of $Au_{21}(S\text{-}Adm)_{15}$ at different applied pressures and the CDDs of S_1 at 0 GPa and 5.0 GPa.

Figure 3B shows how the absorption spectrum changes as a function of pressure. These spectra were calculated by optimizing the crystal structure (atomic coordinates, cell shape, and cell volume) under different applied pressures, extracting a single nanocluster from the unit cell, and performing time-dependent DFT analysis on the resultant structure. It can be seen clearly from these results that an applied pressure is associated with a red shift of the lowest-energy absorption band, akin to what was found experimentally. Importantly, the collection of excitations that form the lowest-energy absorption band appear as a single peak (750 nm, purple line) when taken from the crystal structure (Figure 3B), and splits into multiple bands (715 nm and 845 nm, green line) as pressure is increased to 1.0 GPa. Here, excited-state S_1 is responsible for the red-shifting behavior, while nearby higher ordered excited states, S_2 through S_4 (627 to 697 nm), remain relatively stable or trend upwards in energy, similar to what was observed for pressure-induced PL (Figure 2B). These trends continue to 5.0 GPa. From the insets in Figure 3, the charge difference densities (CDDs) show how electron density moves upon photoexcitation for S_1 in the ground state geometry and excited state geometry (Figure 3A), and for ambient pressure and 5.0 GPa of applied pressure (Figure 3B). The CDDs were taken as the weighted difference between occupied and virtual orbitals involved in the excitation. It can be seen that minimal electronic rearrangement is present from the relaxation of S_1 in the gas phase, but significant distortions are present from an applied pressure including an asymmetric compression of the nuclear geometry that results in some mild separation between electron (yellow) and hole (blue) densities. A more detailed account of excited-state character can be found in the Supporting Information (SI). Ligand flexure was minimal and asymmetric in nature, unlike other nanoclusters reported in the literature that exhibit chiral ligand rotation.[39]

To understand the fundamental cause for the energetic shift in absorption and PL spectra, we consider a simplified model of gold nanoclusters and examine how the electronic structure of some digold and tetragold complexes is affected by pressure changes using DFT. The structures and energetics of these complexes are given in Figures S7 – S12. By performing a frequency calculation on the optimized geometries for these model compounds, a vibrational mode from the

DFT Hessian was identified as corresponding to a breathing mode. This breathing mode was used to scale the atomic coordinates of the model compound so as to simulate the effect of an applied pressure. The results show a high degree of variability between different complexes in terms of how the bandgap is affected by molecular compression (Figure S13); either increasing, decreasing, or remaining constant.

The behavior in Figure S13 arises because a given molecular orbital (MO) may either decrease or increase in energy with applied pressure depending on whether it is predominantly of bonding or antibonding character. This is because the equilibrium bond lengths of the molecule are longer than the equilibrium bond lengths of the component bonding MOs in order to counteract the unfavorable antibonding MOs that also contribute to the total electronic energy. As such, compounds with a bonding HOMO and antibonding LUMO display increasing bandgaps as a function of increasing pressure. Figure S8 shows an example of this behavior, which commonly occurs when the HOMO and LUMO are of the same orbital character. In these cases (*e.g.,* π-π^* excitations), the vertical transition involving these orbitals is symmetry-allowed and gives rise to large absorptivity coefficients and high radiative rates. In addition, absorption and PL will blue-shift under pressure. Indeed, when blue-shifting does not occur, it suggests that the HOMO/LUMO combination does not involve bonding/antibonding orbitals of the same character. This is the case in Figure S7, where a curve crossing leads to a bandgap that is constant close to a scale factor of 1. It can be concluded that the shift in excitation energy in the measured spectra is an indicator of the character of the MOs involved in that excitation. In the case of Au_{21}(S-Adm)$_{15}$, examination of the MOs involved in photoexcitation in Figure S15 and Table S1 shows that the lowest lying excited state S_1 involves a HOMO to LUMO transition in which both MOs are of bonding character and symmetry disallowed. Importantly, discrepancies in the energetic shift between absorption and PL (*e.g.,* red-shifting absorption and blue-shifting PL) indicate that these transitions do not correspond to the same excited state. This can happen when absorption occurs to a state that nonradiatively relaxes to a new state of different orbital character, as seems to be the case with Au_{21}(S-Adm)$_{15}$. In particular, the MO pairing for S_2 of Au_{21}(S-Adm)$_{15}$ is a combination of bonding and antibonding MOs, as shown in Table S1 and Figure S15, necessitating that S_1 and S_2 must display a chromic shift in opposing directions.

2.2. Spectroscopic Study of $Au_{38}S_2(S\text{-}Adm)_{20}$

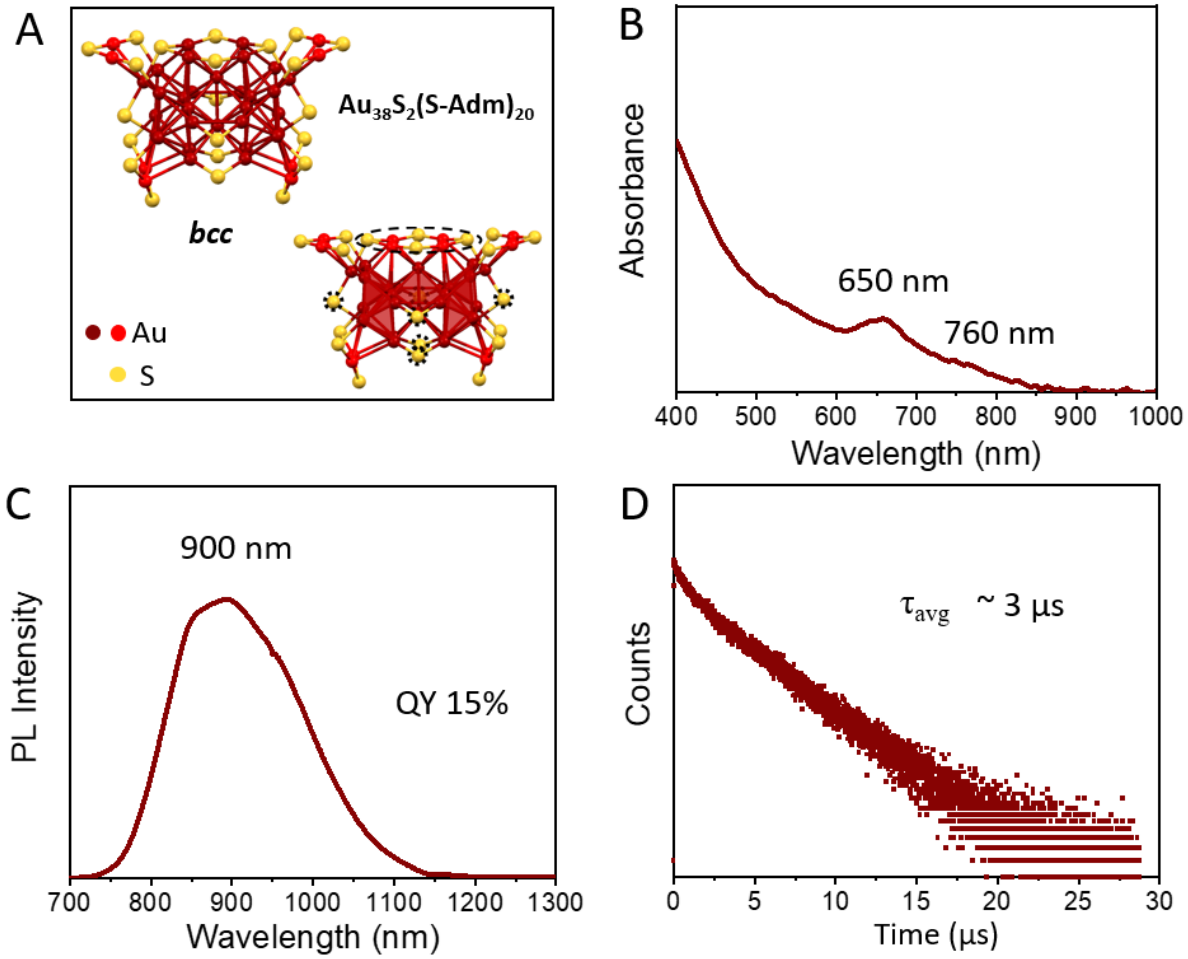

Figure 4. Optical Properties of $Au_{38}S_2(S\text{-}Adm)_{20}$. (A) Atomic structure determined from single-crystal diffraction.[40] (B) Absorption spectrum. (C) PL spectrum (excited at 500 nm). (D) TCSPC trajectory. Samples were dissolved in toluene.

In this section, the optical properties of another nanocluster, *bcc* $Au_{38}S_2(S\text{-}Adm)_{20}$,[40] are presented. The atomic structure of $Au_{38}S_2(S\text{-}Adm)_{20}$ determined from single-crystal diffraction[40] is shown in Figure 4A. $Au_{38}S_2(S\text{-}Adm)_{20}$ is a *bcc* Au_{30} kernel which are protected by 4 Au_2S_3 motifs, two tripodal S atoms (dashed black circles in Figure 4A) and 8 S-bridging thiolates (dashed black circles in Figure 4A). Particularly, a Au_4S_4 surface "lock ring" (dashed black circles in Figure 4A) structure are identified. A previous fs-TA study showed that $Au_{38}S_2(S\text{-}Adm)_{20}$ has a very long excited-state lifetime with no significant state-changing processes from several picosecond to hundreds of nanoseconds.[41] This indicates the absence of fast non-radiative processes, such that high PL efficiency can be expected. This is confirmed by our experimental results (**Figure 4**) that

$Au_{38}S_2(S\text{-}Adm)_{20}$ has a high PL QY up to 15% in toluene. The absorption spectrum of $Au_{38}S_2(S\text{-}Adm)_{20}$ is shown in Figure 4B. A peak at ~ 650 nm with a shoulder around 760 nm are observed. Figure 4C shows the PL spectrum of $Au_{38}S_2(S\text{-}Adm)_{20}$ with a peak at ~ 900 nm. Thus, the Stokes shift of $Au_{38}S_2(S\text{-}Adm)_{20}$ is calculated to be 0.25eV. The QY of $Au_{38}S_2(S\text{-}Adm)_{20}$ is determined to be 12~15% using a rod-shaped Au_{25}[35] and a bi-tetrahedral Au_{24}[10] nanocluster as references.[35] The PL lifetime of $Au_{38}S_2(S\text{-}Adm)_{20}$ was obtained from the TCSPC measurement (Figure 4D), which gave a ~3 μs average lifetime, similar to the lifetime result from nanosecond transient absorption measurement.[41] The optical properties of $Au_{38}S_2(S\text{-}Adm)_{20}$ in DCM are shown in Figure S6, which are similar to the results in toluene. The absorption coefficient (ε) of the 650 nm transition (the most significant absorption peak) of $Au_{38}S_2(S\text{-}Adm)_{20}$ was calculated to be ~2.5 x 10^3. Thus, the ε of the band-edge transition around 760 nm is just ~1x10^3, which is smaller than for $Au_{21}(S\text{-}Adm)_{15}$. Thus, the intrinsic radiative decay of the band-edge transition in $Au_{38}S_2(S\text{-}Adm)_{20}$ should also be slower.

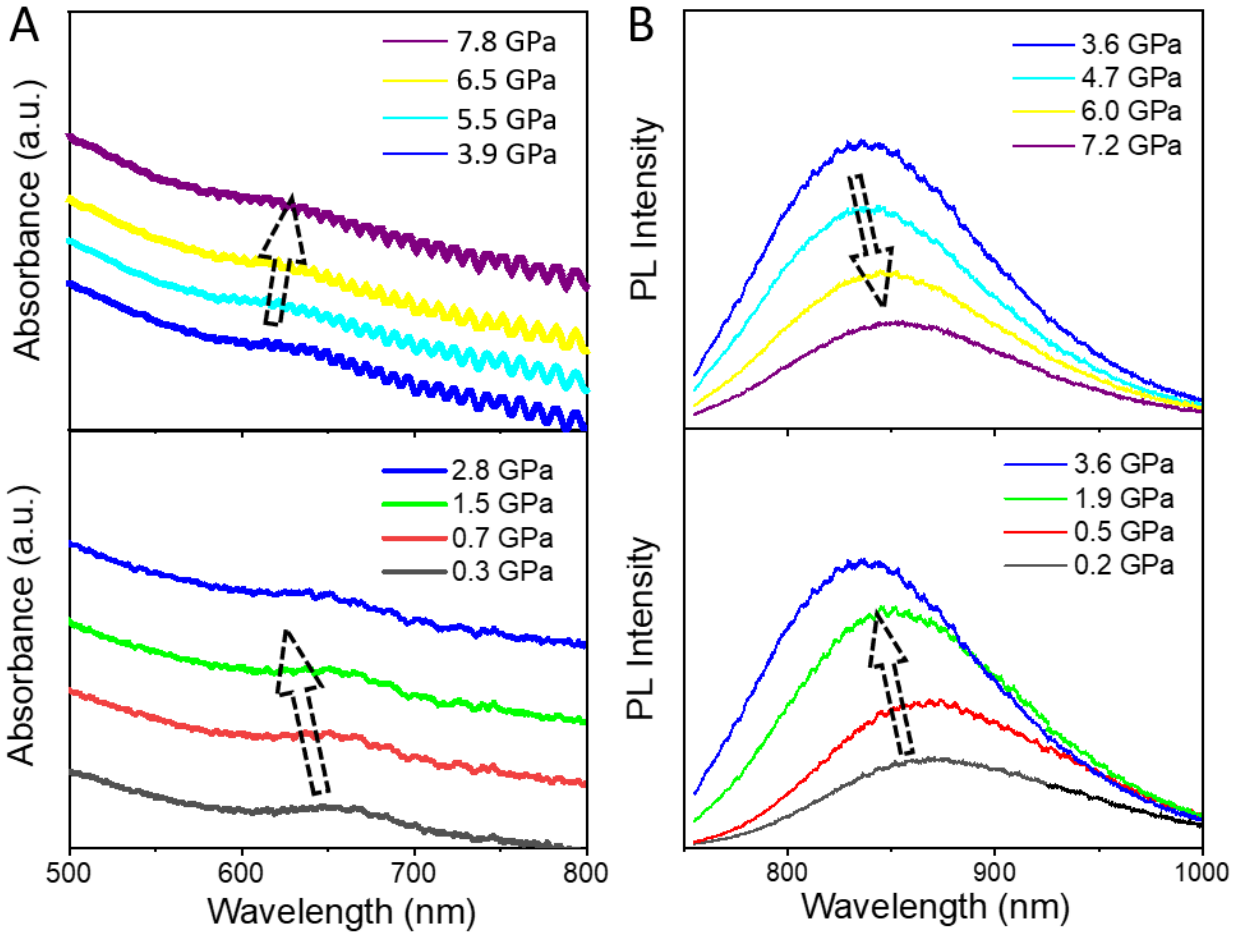

Figure 5. High-Pressure Optical Study of $Au_{38}S_2$(S-Adm)$_{20}$. (A) Pressure-dependent absorption and (B) PL spectra in toluene.

High-pressure optical studies were conducted to further unravel the PL mechanism of the $Au_{38}S_2$(S-Adm)$_{20}$. **Figure 5** displays the pressure-dependent absorption and PL spectra of $Au_{38}S_2$(S-Adm)$_{20}$ which are dissolved in toluene, a non-hydrostatic medium. The absorption peak at ~ 680 nm blue-shifts as the pressure increases from 0.0 to 3.9 GPa. As the pressure further increases, this absorption peak begins to red-shift. The PL shows a similar trend with pressure as absorption, indicating that the underlying transitions of the PL and the absorption at 650 nm are the same.

To elucidate the fundamental differences in the optical properties of Au_{21}(S-Adm)$_{15}$ compared to $Au_{38}S_2$(S-Adm)$_{20}$, DFT analysis was again performed on $Au_{38}S_2$(S-Adm)$_{20}$ (**Figure 6**). The optimized geometry gave an average Au-Au bond length for the *bcc* kernel of 2.83 Å +/- 0.05 Å compared to the 2.75 Å +/- 0.04 Å found from the crystal structure. The minimal error in theoretical bond length of $Au_{38}S_2$(S-Adm)$_{20}$ compared to Au_{21}(S-Adm)$_{15}$ can be attributed to the minimized variability in bond order for Au atoms in the *bcc* kernel in contrast with the *quasi*-cuboctahedral kernel. It can be seen in Figure 6A that $Au_{38}S_2$(S-Adm)$_{20}$ displays a lowest-energy excited state S_1 at 813 nm, in good agreement with the experimental onset of absorption seen in Figure 4A. Additionally, the calculated wavelength of fluorescence was found to be 898 nm, in near-perfect agreement with the experimental PL of 900 nm. This synergy between theory and experiment with $Au_{38}S_2$(S-Adm)$_{20}$ that was not present for Au_{21}(S-Adm)$_{15}$ continues the narrative that S_1 of Au_{21}(S-Adm)$_{15}$ may not be the appropriate state-of-interest for PL. Moreover, the relatively smaller calculated Stokes shift of 0.14 eV for $Au_{38}S_2$(S-Adm)$_{20}$ shows that minimal structural reorganization is present after photoexcitation compared to Au_{21}(S-Adm)$_{15}$. Although the CDD of $Au_{38}S_2$(S-Adm)$_{20}$ does show some distortion upon relaxation of the excited-state geometry (Fig. 6A), similar distortions are also present in the pressure-dependent results of Figure 6B. Here, the calculated absorption spectra blue-shift as a function of pressure from S_1 = 843 nm to S_1 = 822 nm, followed by a reversal towards red-shifting behavior at 2.5 GPa and beyond. Interestingly, the distortions in the CDD of the excited state begins to take on similar character as the optimized excited-state geometry under ambient conditions. However, with sufficient pressure (5.0 GPa), structural rearrangement leads to charge-transfer like states that are much lower in energy. These emergent lower energy states are evident in the midgap region of the density of states shown in

Figure S19 and can explain the reduction in PL intensity at higher pressures (> 3.6 GPa) seen experimentally. From our observations, it appears that the enhancement in PL as a function of pressure results from the conformational locking of the nanocluster in the desired excited-state geometry, thereby increasing PL efficiency by minimizing the amount of energy lost as heat.

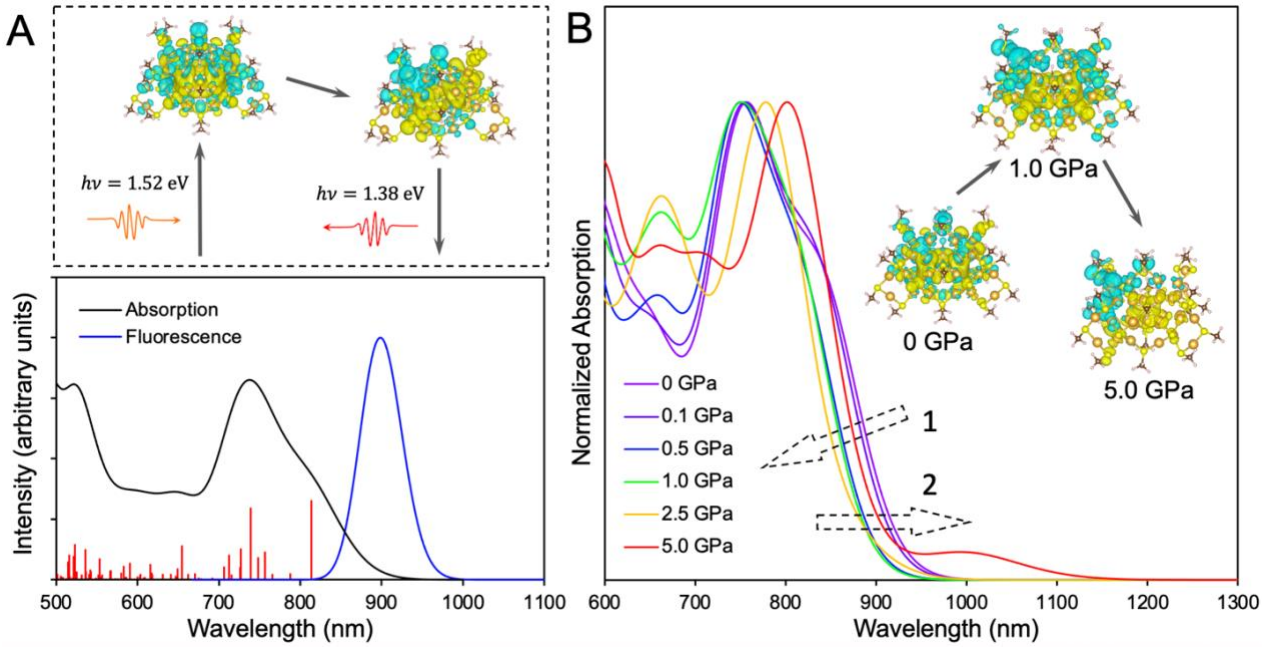

Figure 6. (A) Calculated absorption (black) and fluorescence (blue) spectra of $Au_{38}S_2(S\text{-}Adm)_{20}$ where red lines show the stick spectrum of individual excitations. The top box shows the CDDs of S_1 in the ground state geometry and the relaxed excited-state geometry *via* a simplified Jablonski diagram. (B) Calculated absorption spectra of $Au_{38}S_2(S\text{-}Adm)_{20}$ at different applied pressures and the CDDs of S_1 at 0 GPa and 5.0 GPa.

Drawing on the results of the DFT study on small model Au compounds, it can be seen that there is a fundamental difference in the state-specificity of PL between $Au_{21}(S\text{-}Adm)_{15}$ and $Au_{38}S_2(S\text{-}Adm)_{20}$. Whereas the absorption and PL of $Au_{38}S_2(S\text{-}Adm)_{20}$ both show blue-shifting behavior at low applied pressures, $Au_{21}(S\text{-}Adm)_{15}$ shows opposite trends between absorption and PL with increasing pressure (red-shifting absorption and blue-shifting PL). The results from the model compounds showed that the energetic trends of the band gap with pressure depend directly on the bonding or anti-bonding nature of the frontier MOs. Such a finding can be generalized to larger clusters and to the MOs involved in any excited state. For example, it can be seen from Figure S20 and Table S2 that $Au_{38}S_2(S\text{-}Adm)_{20}$ displays a bonding to anti-bonding S_1 transition, which is symmetry-allowed and should give rise to blue-shifting electronic spectra at low applied

pressures, which is seen experimentally and theoretically. It is easily assumed from here that if the measured absorption and photoluminescence do not have matching trends with respect to pressure, they consequently cannot correspond to the same state. This allows for the conclusion that the lowest-energy excited state of $Au_{38}S_2(S\text{-}Adm)_{20}$ is directly responsible for PL, and its symmetry-allowed transition gives rise to high quantum efficiency, whereas $Au_{21}(S\text{-}Adm)_{15}$ has a lowest-energy excited state that does not correspond directly to PL intensity, leading to a non-radiative decay pathway.

2.3. PL Characteristics and Enhancement in Gold Nanoclusters

We summarize the PL and excited-state features of $Au_{21}(S\text{-}Adm)_{15}$ and $Au_{38}S_2(S\text{-}Adm)_{20}$ in **Scheme 1** and discuss the origins of the observed large Stokes shifts (ΔE) and long PL lifetimes (τ) in gold nanoclusters. Two underlying origins can be summarized for these features. First, the absorption coefficient (ε) of the band-edge transition in $Au_{21}(S\text{-}Adm)_{15}$ and $Au_{38}S_2(S\text{-}Adm)_{20}$ are low; thus, the corresponding intrinsic radiative decay is slow (k_r is small) and the intrinsic radiative lifetime is long. We also measured the absorption coefficient in several other gold nanoclusters and their band-edge ε are almost in the range of $\sim 10^3$ (Table 1) which are one-to-two orders of magnitude lower than quantum dots and organic dyes. Thus, the intrinsic radiative decays are slow in all of these gold nanoclusters. This explains why their measured PL lifetimes are generally from hundreds of ns to several μs. Meanwhile, the low absorption coefficient could make the band-edge transition "invisible" in the absorption spectrum, thus the observed the large Stokes shifts in many nanoclusters are actually the energy difference between higher-energy absorption transition and the PL.[34,35] Secondly, many gold nanoclusters show rich structure-relaxation/transformation processes[10] under excitation and these significant excited-state processes could increase the Stokes shifts.

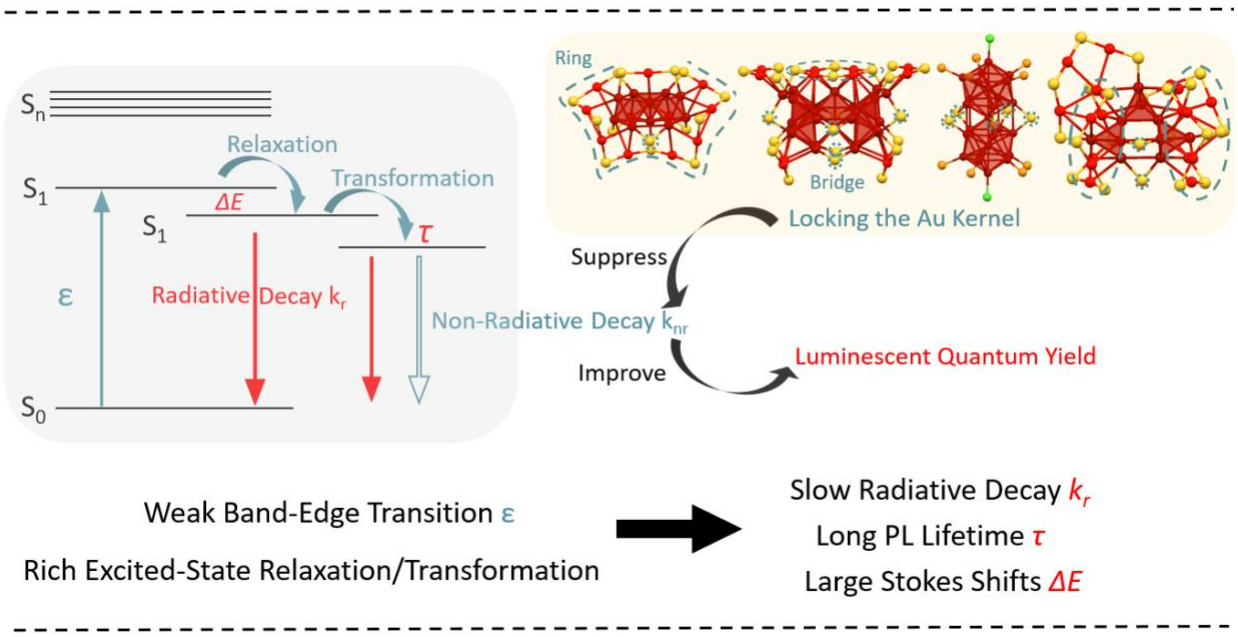

Scheme 1. General PL and Excited-State Characteristics of Gold Nanoclusters.

Table 1. Optical Parameters of $Au_{21}(S\text{-}Adm)_{15}$, $Au_{38}S_2(S\text{-}Adm)_{20}$ and other Gold Nanoclusters.

Nanocluster	Structure	ε	QY	$\tau_{average}$	k_r	k_{nr}
$Au_{38}S_2(S\text{-}Adm)_{20}$	*bcc*	1×10^3	**15%**	3.0 μs	5×10^4	**2.8×10^5**
$Au_{21}(S\text{-}Adm)_{20}$	Quasi-cuboctahedral	5×10^3	**4%**	1.5 μs	2.7×10^4	**6.4×10^5**
$Au_{25}(S\text{-}PET)_5(PPh_3)_{10}X_2$	Bi-icosahedral	$<1\times10^3$	**8%**	3.2 μs	2.5×10^4	**2.9×10^5**
$Au_{23}(S\text{-}cC_6)_{16}$	Cuboctahedral	8.7×10^3	0.4%	0.033 μs	1.33×10^5	3×10^7
$Au_{28}(S\text{-}TBBT)_{20}$	Bi-cuboctahedral	1.2×10^4	0.1%	0.158 μs	6.3×10^3	6.3×10^6
$Au_{24}(S\text{-}PET)_5(PPh_3)_{10}X_2$	Bi-icosahedral	$<1\times10^3$	1%	0.3 μs	3.3×10^4	3.3×10^6

Note: Part of the data for $Au_{25}(S\text{-}PET)_5(PPh_3)_{10}Cl_2$ (S-PET=2-Phenylethanethiol; PPh= triphenylphosphine; X = Cl or Br;), $Au_{23}(S\text{-}cC_6)_{16}$ (S-cC_6=cyclohexanethiol),[12] $Au_{28}(S\text{-}TBBT)_{20}$[11] (S-TBBT=4-tertbenzenethiol) and $Au_{24}(S\text{-}PET)_5(PPh_3)_{10}Cl_2$[35] are from literature sources.[11,12,35]

So far, $Au_{38}S_2(S\text{-}Adm)_{20}$ shows the highest QY among Au-thiolate nanoclusters in normal solvents and ambient environment. From the measured PL QY (15%) and lifetime (3 μs in average), the k_r and k_{nr} of $Au_{38}S_2(S\text{-}Adm)_{20}$ can be calculated as 5×10^4 s^{-1} and 2.8×10^5 s^{-1} based on the following equations: $\tau = 1/(k_r + k_{nr})$; $QY = k_r/(k_r + k_{nr})$. In $Au_{21}(S\text{-}Adm)_{15}$, although the excited-state transition rate is 1/1.2 ns = 8.3×10^8 s^{-1} which is quite fast, the radiative and non-radiative

decay rates back to the ground-state are calculated to be 2.7×10^4 s^{-1} and 6.4×10^5 s^{-1}. In addition, we recently reported that the rod-shaped Au_{25} nanocluster shows a QY up to 8% and its k_r and k_{nr} are 2.5×10^4 s^{-1} and 2.9×10^5 s^{-1}, respectively.[35] In other Au-thiolate nanoclusters with lower QY, for example, Au_{23}(S-*c*C_6)$_{16}$ (QY 0.4 %), the k_r and k_{nr} of are 1.33×10^5 s^{-1} and 3×10^7 s^{-1};[12] the k_r and k_{nr} of Au_{28}(S-TBBT)$_{20}$ (QY 0.1 %) are $0.63\times10^4 s^{-1}$ and 6.32×10^6 s^{-1};[11] These results suggest that in Au-thiolate nanoclusters which have intrinsic slow radiative decays, the key to obtaining a high PL QY lies in the suppression of the non-radiative decays.

In $Au_{38}S_2$(S-Adm)$_{20}$, the Au_{30} kernel is fixed by two "tripodal" S atoms and eight bridging thiolates, in which every S connects two fundamental Au-kernel tetrahedral units. Meanwhile, the Au_4S_4 ring can further "lock" the Au_{30} kernel. In the Au_{21}(S-Adm)$_{15}$, one S atom bridges two Au tetrahedra and the Au_8S_9 ring further fixes the nanocluster. In the rod-shaped Au_{25}, the five surface S atom and the central gold atom act as the lock atoms which bridge the two icosahedral units.[35] We also note that the Wu group recently published a Au_{28} nanocluster with a 650 nm visible emission and a 5% QY,[42] where two Au_6S_6 lock-rings and two bridging thiolates (lock atoms) are observed in the structure (scheme 1). The Zhu group recently reported the PL of Au_{22}(S-Adm)$_{16}$ which has the same Au_8S_9 surface-ring with a surface locking S atom as the Au_{21}(S-Adm)$_{15}$ and based on their measurements, Au_{22}(S-Adm)$_{16}$ nanocluster shows a higher PL efficiency than Au_{21}(S-Adm)$_{15}$.[43] In addition, the Xie group reported another Au_{22} nanocluster with a 8 % QY and it also has Au_4S_5 surface ring-like motifs.[44] In contrast, Au-thiolate nanoclusters with low PL QY (*e.g.,* Au_{23}(S-*c*C_6)$_{16}$,[12] Au_{28}(S-TBBT)$_{20}$,[11] *etc.*) are normally protected by short and linear Au_nS_{n+1} surface motifs. Thus, we envision that the surface Au-S "lock rings" which encircle the Au kernel and the surface sulfur "lock atoms" which bridge the fundamental Au-kernel units (*e.g.,* tetrahedra, icosahedra, *etc.*) can fix the Au kernel and suppress the non-radiative motion which significantly enhances the QY of the different structural series of gold nanoclusters. It should be noted that besides the surface Au-S geometry, the suppression of non-radiative decay can also be influenced by the type of organic ligand as different ligands have different rigidity.

3. Conclusions

In summary, a QY up to 15% is found from $Au_{38}S_2$(S-Adm)$_{20}$, which to our best knowledge, is the highest reported QY in luminescent Au-thiolate nanoclusters in normal solvents and ambient conditions. A rare emission from a nearby non-S_1 state is observed in Au_{21}(S-Adm)$_{15}$ which is verified by both the high-pressure optical study and DFT calculations. More importantly, this work

reveals that the existence of "lock rings" and "lock atoms" is the key to obtain higher QYs in Au-thiolate nanoclusters, and the suppression of non-radiative symmetry-forbidden states leads to maximal PL efficiency. Last but not least, our results also reveals that the weak band-edge transition and rich excited state transition/transformations are the two fundamental origins for the common PL characteristics (*e.g.,* large Stokes shifts and long PL lifetime) in gold nanoclusters. Overall, these insights on the underlying origins of the common PL characteristics and enhancement will benefit precise control and optimization of PL in gold and other metal nanoclusters.

4. Methods and Materials

Synthesis of Nanoclusters. The synthesis of the Au_{21}(S-Adm)$_{15}$ and $Au_{38}S_2$(S-Adm)$_{20}$ followed previously reported methods.[36,40]

Optical Measurements. UV–vis absorption measurements were taken in a home-built system. A halogen lamp (15 V, 150 W, 3100 K) was chosen as the white light source and a flame detector 200–1000 nm (Ocean Optics, Inc.) was used as the detector. NIR absorption was taken in an Agilent Cary 6000i Spectrophotometer. PL and TCSPC spectra were measured using a Horiba FluoroLog-3 spectrometer which is equipped with a R2658P detector (250-1050 nm) and a thermoelectric cooled NIR detector (950 nm to 1700 nm). PL spectra were also measured using a Horiba XploRA+ confocal raman microscope.

Ultrafast Transient Absorption. Samples were prepared in toluene to have an optical density of 0.6 in a 2 mm pathlength quartz cuvette. An Astrella Ti:Sapphire amplifier from Coherent was used as a light source, which operates at a 1 kHz repetition rate, generating 120 fs pulses at 800 nm. The 800 nm fundamental was split into two beams, one to be used as an excitation (pump) source and the other for probing. The pump beam was guided into an optical parametric amplifier supplied by Coherent where the wavelength was tuned to 380 nm. Both beams were then directed into a Helios Femtosecond Transient Absorption Spectrometer (Ultrafast Systems, LLC) where the 380 nm pump was passed through a chopper, reducing its repetition rate by half, and a neutral density filter was used to adjust the average power to 0.10 mW (100 nJ/pulse). The probe beam was then guided through a digitally-controlled delay stage with a maximum range of 8 ns before being passed through a sapphire plate for white light generation. The two beams were then overlapped at the sample position with their respective electronic polarizations at the magic angle. Absorption difference spectra were then generated by collecting an absorption spectrum with and without

pumping through a fiber-coupled spectrometer at specific time delay several thousand times and averaging the results. This process was repeated at several hundred different time delays to produce an array of absorption difference spectra. Time-zero, solvent response, and chirp corrections were employed using software supplied by Ultrafast Systems. Sufficient output power from the Astrella was dumped so as not to damage optics.

In situ high-pressure absorption and PL measurements. Absorption measurements were taken on a home-built Nikon microscope system using 10× objective. For the absorption measurements, a halogen lamp (15 V, 150 W, 3,100 K) was chosen as the white light source. The flame detector 200–1,000 nm (Ocean Optics, Inc) was used as the detector. PL spectra were measured using both the Nikon microscope system and the Horiba XploRA+ confocal Raman setup using 10× objective. Samples were excited by a 532 nm or 638 nm laser and the fluorescent signal was collected using a 600 gr/mm diffraction grating

Computational Methods. For absorption spectra under ambient conditions, alkyl ligands were reduced to methyl groups to alleviate computational cost and geometries were optimized with the BP86 exchange-correlation functional.[45,46] The def2-SVP basis set was used for Au and SV basis functions for all other atoms.[47,48] Linear response TDDFT was performed at the same level of theory on the resultant structure for 120 singlet excitations and utilized a Tamm-Dancoff and Davidson threshold of 10^{-5}. These excitations were convoluted with Gaussian functions (FWHM = .16 eV to fit experimental data) to produce the reported spectra. For PL energies, the lowest lying excited state, S_1, was optimized and the discussed methodology for calculating the $E_{0\text{-}0}$ transition was used.[38] For this purpose, zero-point vibrational corrections were assumed to be negligible. All calculations were done with a frozen core, in vacuum, and without symmetry constraints.

For pressure simulations, the experimental unit cell (800 to 1900 atoms) from X-ray crystallography data was optimized (nuclear coordinates, cell shape, and cell volume) using plane-wave DFT. The PBE exchange correlation functional[49] was used in conjunction with frozen core pseudopotentials for all atoms. Only the gamma point was used for k-point sampling. External pressure was then applied to the unit cell in the form of Pulay stress and reoptimized. This process was repeated sequentially (0.1 GPa, 0.5 GPa, 1.0 GPa, 2.5 GPa, and 5.0 GPa) in order to produce a series of crystal structures at different pressures. These optimized structures were then used as input for optimization at an increased level of theory (2x2x2 Monkhorst-Pack mesh of k-points).

Each unit cell contained multiple distinct nanocluster structures (2 to 8 nanoclusters per unit cell). Each of these NCs were extracted from the optimized unit cell at different pressures and the alkyl ligands were trimmed to methyl groups. Such simplifications of ligand structure have been shown to have minimal impact on the electronic structure in gold-containing chromophores.[50–52] For comparison, the computational results on the complete structure of Au_{21}(S-Adm)$_{15}$ are given in the SI. Hydrogen atoms were then optimized while keeping all other atoms frozen and TDDFT analysis was performed on the resultant structures using the same methodology as described for ambient conditions. The calculated absorption spectra for different nanoclusters at a specific pressure were then averaged to produce the final spectrum at that pressure.

All calculations done on the crystal structure were conducted in the Vienna *Ab Initio* Simulation Package (VASP, v. 5.4.4)[53–55] and all calculations on single molecules in the gas phase were done using ORCA (v. 4.0.1).[56]

Supporting Information

Additional ambient absorption and PL spectra, pressure-dependent spectra, and DFT results, including molecular orbital analysis of model compounds, excited-state and molecular orbital analysis, and density of states of the metal nanoclusters under pressures.

Acknowledgements

Q.L., X.W.G., C.J.Z., and G.C.S. acknowledge National Science Foundation (NSF) grant DMR-2002936/2002891. Part of this work was performed at the Stanford Nano Shared Facilities (SNSF), which is supported by the National Science Foundation under award ECCS-1542152. C.J.Z., and G.C.S. were supported by DOE grant DE-AC02-06CH11357 for theory development. This research was supported in part through the computational resources and staff contributions provided for the Quest high-performance computing facility at Northwestern University which is jointly supported by the Office of the Provost, the Office for Research, and Northwestern University Information Technology.

Author Contributions

Q.L., and C.J.Z contributed equally.

Corresponding Authors

Qi Li qilistan@stanford.edu and X. Wendy Gu xwgu@stanford.edu

Conflict of Interest

The authors declare no conflict of interest.

References

(1) Jin, R.; Zeng, C.; Zhou, M.; Chen, Y. Atomically Precise Colloidal Metal Nanoclusters and Nanoparticles: Fundamentals and Opportunities. *Chem. Rev.* **2016**, *116* (18), 10346–10413.

(2) Aikens, C. M. Electronic and Geometric Structure, Optical Properties, and Excited State Behavior in Atomically Precise Thiolate-Stabilized Noble Metal Nanoclusters. *Acc. Chem. Res.* **2018**, *51* (12), 3065–3073.

(3) Krishnadas, K. R.; Sementa, L.; Medves, M.; Fortunelli, A.; Stener, M.; Fürstenberg, A.; Longhi, G.; Bürgi, T. Chiral Functionalization of an Atomically Precise Noble Metal Cluster: Insights into the Origin of Chirality and Photoluminescence. *ACS Nano* **2020**, *14* (8), 9687–9700.

(4) Han, X.-S.; Luan, X.; Su, H.-F.; Li, J.-J.; Yuan, S.-F.; Lei, Z.; Pei, Y.; Wang, Q.-M. Structure Determination of Alkynyl-Protected Gold Nanocluster Au22(TBuC≡C)18 and Its Thermochromic Luminescence. *Angew. Chem. Int. Ed.* **2020**, *59* (6), 2309–2312.

(5) Lei, Z.; Pei, X.-L.; Guan, Z.-J.; Wang, Q.-M. Full Protection of Intensely Luminescent Gold(I)–Silver(I) Cluster by Phosphine Ligands and Inorganic Anions. *Angew. Chem. Int. Ed.* **2017**, *56* (25), 7117–7120.

(6) Yang, J.-S.; Han, Z.; Dong, X.-Y.; Luo, P.; Mo, H.-L.; Zang, S.-Q. Extra Silver Atom Triggers Room-Temperature Photoluminescence in Atomically Precise Radarlike Silver Clusters. *Angew. Chem. Int. Ed.* **2020**, *59* (29), 11898–11902.

(7) Han, Z.; Dong, X.-Y.; Luo, P.; Li, S.; Wang, Z.-Y.; Zang, S.-Q.; Mak, T. C. W. Ultrastable Atomically Precise Chiral Silver Clusters with More than 95% Quantum Efficiency. *Sci. Adv.* **2020**, *6* (6), eaay0107.

(8) Chakraborty, I.; Pradeep, T. Atomically Precise Clusters of Noble Metals: Emerging Link between Atoms and Nanoparticles. *Chem. Rev.* **2017**, *117* (12), 8208–8271.

(9) Kang, X.; Zhu, M. Tailoring the Photoluminescence of Atomically Precise Nanoclusters. *Chem. Soc. Rev.* **2019**, *48* (8), 2422–2457.

(10) Li, Q.; Zhou, D.; Chai, J.; So, W. Y.; Cai, T.; Li, M.; Peteanu, L. A.; Chen, O.; Cotlet, M.; Wendy Gu, X.; Zhu, H.; Jin, R. Structural Distortion and Electron Redistribution in Dual-Emitting Gold Nanoclusters. *Nat. Commun.* **2020**, *11* (1), 2897.

(11) Chen, Y.; Zhou, M.; Li, Q.; Gronlund, H.; Jin, R. Isomerization-Induced Enhancement of Luminescence in Au 28 (SR) 20 Nanoclusters. *Chem. Sci.* **2020**, *11* (31), 8176–8183.

(12) Li, Q.; Zhou, M.; So, W. Y.; Huang, J.; Li, M.; Kauffman, D. R.; Cotlet, M.; Higaki, T.; Peteanu, L. A.; Shao, Z.; Jin, R. A Mono-Cuboctahedral Series of Gold Nanoclusters: Photoluminescence Origin, Large Enhancement, Wide Tunability, and Structure–Property Correlation. *J. Am. Chem. Soc.* **2019**, *141* (13), 5314–5325.

(13) Shichibu, Y.; Konishi, K. HCl-Induced Nuclearity Convergence in Diphosphine-Protected Ultrasmall Gold Clusters: A Novel Synthetic Route to “Magic-Number” Au13 Clusters. *Small* **2010**, *6* (11), 1216–1220.

(14) Wan, X.-K.; Xu, W. W.; Yuan, S.-F.; Gao, Y.; Zeng, X.-C.; Wang, Q.-M. A Near-Infrared-Emissive Alkynyl-Protected Au24 Nanocluster. *Angew. Chem. Inter. Ed.* **2015**, *54* (33), 9683–9686.

(15) Pyo, K.; Thanthirige, V. D.; Kwak, K.; Pandurangan, P.; Ramakrishna, G.; Lee, D. Ultrabright Luminescence from Gold Nanoclusters: Rigidifying the Au(I)–Thiolate Shell. *J. Am. Chem. Soc.* **2015**, *137* (25), 8244–8250.

(16) Liu, H.; Hong, G.; Luo, Z.; Chen, J.; Chang, J.; Gong, M.; He, H.; Yang, J.; Yuan, X.; Li, L.; Mu, X.; Wang, J.; Mi, W.; Luo, J.; Xie, J.; Zhang, X.-D. Atomic-Precision Gold Clusters for NIR-II Imaging. *Advanced Materials 0* (0), 1901015.

(17) Song, X.; Zhu, W.; Ge, X.; Li, R.; Li, S.; Chen, X.; Song, J.; Xie, J.; Chen, X.; Yang, H. A New Class of NIR-II Gold Nanocluster-Based Protein Biolabels for In Vivo Tumor-Targeted Imaging. *Angew. Chem. Int. Ed.* **2021,** *60,* 1306 –1312.

(18) Du, B.; Jiang, X.; Das, A.; Zhou, Q.; Yu, M.; Jin, R.; Zheng, J. Glomerular Barrier Behaves as an Atomically Precise Bandpass Filter in a Sub-Nanometre Regime. *Nat. Nanotechnol.* **2017**, *12* (11), 1096–1102.

(19) Liu, J.; Yu, M.; Ning, X.; Zhou, C.; Yang, S.; Zheng, J. PEGylation and Zwitterionization: Pros and Cons in the Renal Clearance and Tumor Targeting of Near-IR-Emitting Gold Nanoparticles. *Angew. Chem. Int. Ed.* **2013**, *52* (48), 12572–12576.

(20) Wang, S.; Meng, X.; Das, A.; Li, T.; Song, Y.; Cao, T.; Zhu, X.; Zhu, M.; Jin, R. A 200-Fold Quantum Yield Boost in the Photoluminescence of Silver-Doped AgxAu25−x Nanoclusters: The 13 Th Silver Atom Matters. *Angew. Chem. Int. Ed.* **2014**, *53* (9), 2376–2380.

(21) Suyama, M.; Takano, S.; Tsukuda, T. Synergistic Effects of Pt and Cd Codoping to Icosahedral Au13 Superatoms. *J. Phys. Chem. C* **2020**, *124* (43), 23923–23929.

(22) Soldan, G.; Aljuhani, M. A.; Bootharaju, M. S.; AbdulHalim, L. G.; Parida, M. R.; Emwas, A.-H.; Mohammed, O. F.; Bakr, O. M. Gold Doping of Silver Nanoclusters: A 26-Fold Enhancement in the Luminescence Quantum Yield. *Angew. Chem. Int. Ed.* **2016**, *55* (19), 5749–5753.

(23) Crawford, S. E.; Hartmann, M. J.; Millstone, J. E. Surface Chemistry-Mediated Near-Infrared Emission of Small Coinage Metal Nanoparticles. *Acc. Chem. Res.* **2019**, *52* (3), 695–703.

(24) Ito, S.; Takano, S.; Tsukuda, T. Alkynyl-Protected Au22(C≡CR)18 Clusters Featuring New Interfacial Motifs and R-Dependent Photoluminescence. *J. Phys. Chem. Lett.* **2019**, *10* (21), 6892–6896.

(25) Xia, N.; Yuan, J.; Liao, L.; Zhang, W.; Li, J.; Deng, H.; Yang, J.; Wu, Z. Structural Oscillation Revealed in Gold Nanoparticles. *J. Am. Chem. Soc.* **2020**, *142* (28), 12140–12145.

(26) Wu, Z.; Yao, Q.; Zang, S.; Xie, J. Aggregation-Induced Emission in Luminescent Metal Nanoclusters. *Natl Sci Rev*. **2021**, 8, nwaa208.

(27) Kang, X.; Wang, S.; Zhu, M. Observation of a New Type of Aggregation-Induced Emission in Nanoclusters. *Chem. Sci.* **2018**, *9* (11), 3062–3068.

(28) Sugiuchi, M.; Maeba, J.; Okubo, N.; Iwamura, M.; Nozaki, K.; Konishi, K. Aggregation-Induced Fluorescence-to-Phosphorescence Switching of Molecular Gold Clusters. *J. Am. Chem. Soc.* **2017**, *139* (49), 17731–17734.

(29) Gan, Z.; Liu, Y.; Wang, L.; Jiang, S.; Xia, N.; Yan, Z.; Wu, X.; Zhang, J.; Gu, W.; He, L.; Dong, J.; Ma, X.; Kim, J.; Wu, Z.; Xu, Y.; Li, Y.; Wu, Z. Distance Makes a Difference in Crystalline Photoluminescence. *Nat. Commun.* **2020**, *11* (1), 5572.

(30) Narouz, M. R.; Takano, S.; Lummis, P. A.; Levchenko, T. I.; Nazemi, A.; Kaappa, S.; Malola, S.; Yousefalizadeh, G.; Calhoun, L. A.; Stamplecoskie, K. G.; Häkkinen, H.; Tsukuda, T.; Crudden, C. M. Robust, Highly Luminescent Au13 Superatoms Protected by N-Heterocyclic Carbenes. *J. Am. Chem. Soc.* **2019**, *141* (38), 14997–15002.

(31) Weerawardene, K. L. D. M.; Häkkinen, H.; Aikens, C. M. Connections Between Theory and Experiment for Gold and Silver Nanoclusters. *Annual Review of Physical Chemistry* **2018**, *69* (1), 205–229.

(32) Weerawardene, K. L. D. M.; Aikens, C. M. Theoretical Insights into the Origin of Photoluminescence of Au25(SR)18– Nanoparticles. *J. Am. Chem. Soc.* **2016**, *138* (35), 11202–11210.

(33) Li, Q.; Luo, T.-Y.; Taylor, M. G.; Wang, S.; Zhu, X.; Song, Y.; Mpourmpakis, G.; Rosi, N. L.; Jin, R. Molecular “Surgery” on a 23-Gold-Atom Nanoparticle. *Science Advances* **2017**, *3* (5), e1603193.

(34) Li, Q.; Mosquera, M. A.; Jones, L. O.; Parakh, A.; Chai, J.; Jin, R.; Schatz, G. C.; Gu, X. W. Pressure-Induced Optical Transitions in Metal Nanoclusters. *ACS Nano* **2020**. 14 (9) 11888−11896.

(35) Li, Q.; Zeman, C. J.; Ma, Z.; Schatz, G. C.; Gu, X. W. Bright NIR-II Photoluminescence in Rod-Shaped Icosahedral Gold Nanoclusters. *Small* **2021**, *17* (11), 2007992.

(36) Chen, S.; Xiong, L.; Wang, S.; Ma, Z.; Jin, S.; Sheng, H.; Pei, Y.; Zhu, M. Total Structure Determination of Au21(S-Adm)15 and Geometrical/Electronic Structure Evolution of Thiolated Gold Nanoclusters. *J. Am. Chem. Soc.* **2016**, *138* (34), 10754–10757.

(37) Winter, N. O. C.; Graf, N. K.; Leutwyler, S.; Hättig, C. Benchmarks for 0–0 Transitions of Aromatic Organic Molecules: DFT/B3LYP, ADC(2), CC2, SOS-CC2 and SCS-CC2 Compared to High-Resolution Gas-Phase Data. *Phys. Chem. Chem. Phys.* **2013**, *15* (18), 6623–6630.

(38) Wang, J.; Durbeej, B. How Accurate Are TD-DFT Excited-State Geometries Compared to DFT Ground-State Geometries? *Journal of Computational Chemistry* **2020**, *41* (18), 1718–1729.

(39) Yoon, B.; Luedtke, W. D.; Barnett, R. N.; Gao, J.; Desireddy, A.; Conn, B. E.; Bigioni, T.; Landman, U. Hydrogen-Bonded Structure and Mechanical Chiral Response of a Silver Nanoparticle Superlattice. *Nature Materials* **2014**, *13* (8), 807–811.

(40) Liu, C.; Li, T.; Li, G.; Nobusada, K.; Zeng, C.; Pang, G.; Rosi, N. L.; Jin, R. Observation of Body-Centered Cubic Gold Nanocluster. *Angew. Chem. Int. Ed.* **2015**, *54* (34), 9826–9829.

(41) Zhou, M.; Higaki, T.; Hu, G.; Sfeir, M. Y.; Chen, Y.; Jiang, D.; Jin, R. Three-Orders-of-Magnitude Variation of Carrier Lifetimes with Crystal Phase of Gold Nanoclusters. *Science* **2019**, *364* (6437), 279–282.

(42) Wu, Z.; Dong, J.; Gan, Z.; Gu, W.; You, Q.; Zhao, Y.; Zha, J.; Li, J.; Deng, H.; Yan, N. Synthesizing Photoluminescent Au28(SCH2Ph-TBu)22 Nanoclusters with Feature Structures by Using A Joint Method. *Angew. Chem. Int. Ed.* **2021,** *60,* 17932–17936.

(43) Li, Q.; Yang, S.; Chen, T.; Jin, S.; Chai, J.; Zhang, H.; Zhu, M. Structure Determination of a Metastable Au22(SAdm)16 Nanocluster and Its Spontaneous Transformation into Au21(SAdm)15. *Nanoscale* **2020**, *12* (46), 23694–23699.

(44) Yu, Y.; Luo, Z.; Chevrier, D. M.; Leong, D. T.; Zhang, P.; Jiang, D.; Xie, J. Identification of a Highly Luminescent Au22(SG)18 Nanocluster. *J. Am. Chem. Soc.* **2014**, *136* (4), 1246–1249.

(45) Becke, A. D. Density-Functional Exchange-Energy Approximation with Correct Asymptotic Behavior. *Phys. Rev. A* **1988**, *38* (6), 3098–3100.

(46) Perdew, J. P. Density-functional approximation for the correlation energy of the inhomogeneous electron gas Phys. Rev. B **1986** 33, 8822(R).

(47) Weigend, F.; Ahlrichs, R. Balanced Basis Sets of Split Valence, Triple Zeta Valence and Quadruple Zeta Valence Quality for H to Rn: Design and Assessment of Accuracy. *Phys. Chem. Chem. Phys.* **2005**, *7* (18), 3297–3305.

(48) Weigend, F. Accurate Coulomb-Fitting Basis Sets for H to Rn. *Phys. Chem. Chem. Phys.* **2006**, *8* (9), 1057–1065.

(49) Perdew, J. P.; Burke, K.; Ernzerhof, M. Generalized Gradient Approximation Made Simple. *Phys. Rev. Lett.* **1996**, *77* (18), 3865–3868.

(50) Zhu, M.; Aikens, C. M.; Hollander, F. J.; Schatz, G. C.; Jin, R. Correlating the Crystal Structure of A Thiol-Protected Au25 Cluster and Optical Properties. *J. Am. Chem. Soc.* **2008**, *130* (18), 5883–5885.

(51) Zeman, C. J.; Shen, Y.-H.; Heller, J. K.; Abboud, K. A.; Schanze, K. S.; Veige, A. S. Excited-State Turn-On of Aurophilicity and Tunability of Relativistic Effects in a Series of Digold Triazolates Synthesized via IClick. *J. Am. Chem. Soc.* **2020**, *142* (18), 8331–8341.

(52) Vuong, V. Q.; Madridejos, J. M. L.; Aradi, B.; Sumpter, B. G.; Metha, G. F.; Irle, S. Density-Functional Tight-Binding for Phosphine-Stabilized Nanoscale Gold Clusters. *Chem. Sci.* **2020**, *11* (48), 13113–13128.

(53) Kresse, G.; Hafner, J. Ab Initio Molecular Dynamics for Liquid Metals. *Phys. Rev. B* **1993**, *47* (1), 558–561.
(54) Kresse, G.; Furthmüller, J. Efficient Iterative Schemes for Ab Initio Total-Energy Calculations Using a Plane-Wave Basis Set. *Phys. Rev. B* **1996**, *54* (16), 11169–11186.
(55) Kresse, G.; Joubert, D. From Ultrasoft Pseudopotentials to the Projector Augmented-Wave Method. *Phys. Rev. B* **1999**, *59* (3), 1758–1775.
(56) Neese, F. Software Update: The ORCA Program System, Version 4.0. *Wiley Interdisciplinary Reviews: Computational Molecular Science* **2018**, *8* (1), e1327.